Planetary and Space Science 70 (2012) 134–147

Contents lists available at SciVerse ScienceDirect

Planetary and Space Science

journal homepage: www.elsevier.com/locate/pss

Search for ultraviolet luminescence of soil particles at the Phoenix landing site, Mars

W. Goetz [a,*], M.H. Hecht [b], S.F. Hviid [a], M.B. Madsen [c], W.T. Pike [d], U. Staufer [e], M.A. Velbel [f], N.H. Harrit [g], E. Zych [h], K.S. Edgett [i]

[a] Max-Planck-Institut für Sonnensystemforschung, 37191 Katlenburg-Lindau, Germany
[b] Jet Propulsion Laboratory, Caltech, Pasadena, CA, USA
[c] Niels Bohr Institute, University of Copenhagen, Copenhagen, Denmark
[d] Department of Electrical and Electronic Engineering, Imperial College London, UK
[e] Micro and Nano Engineering Laboratory, TU Delft, Delft, The Netherlands
[f] Department of Geological Sciences, Michigan State University, East Lansing, MI, USA
[g] Department of Chemistry, University of Copenhagen, Nano Science Center, Copenhagen, Denmark
[h] Faculty of Chemistry, University of Wroclaw, Wroclaw, Poland
[i] Malin Space Science Systems, San Diego, CA, USA

ARTICLE INFO

Article history:
Received 3 December 2011
Received in revised form
1 May 2012
Accepted 2 May 2012
Available online 11 May 2012

Keywords:
Mars
Soil particles
UV-excited luminescence
Phoenix
Optical microscope (OM)
Mars hand lens imager (MAHLI)

ABSTRACT

The Optical Microscope (OM) on the Phoenix Mars lander (operated from May through October 2008) was used to search for visible-wavelength luminescence of soil particles excited by ultraviolet (UV) illumination (λ=360–390 nm). No luminescent particles were found, with the possible exception of a few potentially luminescent features comprising about 0.02% of the total soil volume. The luminescence quantum efficiency of bulk soil as well as individual soil particles at the Phoenix site is constrained to less than 0.04%. A similar UV experiment will be performed by the Mars Hand Lens Imager (MAHLI) on the upcoming Mars Science Laboratory (MSL) mission. We compare OM and MAHLI UV experiments to each other and suggest a strategy to search for UV-excited luminescence with MAHLI.

1. Introduction

This paper discusses the Phoenix (PHX) Optical Microscope (OM) ultraviolet (UV) experiment, extending earlier analyses of OM color images. Those analyses led to a descriptive taxonomy of Phoenix soil particles based on their size, shape, color and visible reflectance properties (Goetz et al., 2010a). In the present paper we also include a brief discussion of the UV experiment to be performed by the Mars Hand Lens Imager (MAHLI) onboard Mars Science Laboratory (MSL) and provide general recommendations for future in-situ Mars UV experiments.

The OM UV experiment consisted of illuminating Martian soil with near-ultraviolet (near-UV) radiation and searching for visible (VIS) luminescent emission. The term "luminescence" (here used synonymously with "photo-luminescence") designates a process by which one form of electromagnetic radiation (often UV) stimulates the emission of light of some other type (usually of longer wavelength). Luminescence can occur as fluorescence or as phosphorescence depending on whether the decay time is short or long. Solid-state physicists set the boundary between the two phenomena at ~1 μs, thereby distinguishing allowed and forbidden radiative (electronic) transitions. However, in mineralogy the boundary is generally set at ~0.1 s such that phosphorescence ("afterglow") can just be resolved by the human eye (Gaft et al., 2005; Gorobets and Rogojine, 2002). It is the latter definition that is adopted here. As an example, the luminescent (fluorescent) material BAM ($BaMgAl_{10}O_{17}:Eu^{2+}$) that is used in the OM UV calibration target (Hecht et al., 2008) has a decay time of ~1.1 μs (Zych et al., 2004). The OM UV experiment only addresses potential luminescence of soil particles and cannot distinguish between fluorescence and phosphorescence.

UV-excited luminescence of minerals is most often caused by trace abundances of cations (so-called activators) such as Mn^{2+}, Cr^{3+}, rare-earth elements (Ce^{3+}, Dy^{3+}, Eu^{2+}) and specifically the complex cation UO_2^{2+}. Other causes are traces of organic materials and point defects in crystal lattices (Warren et al., 1995).

* Corresponding author. Tel.: +49 5556 979 463.
E-mail address: goetz@mps.mpg.de (W. Goetz).

0032-0633/$ - see front matter © 2012 Elsevier Ltd. All rights reserved.
http://dx.doi.org/10.1016/j.pss.2012.05.002

Most organic material appears to be luminescent in some sense. In particular, polycyclic aromatic molecules (Table 1) are relevant to the type of luminescence studied here, since they can be excited by UV (typically in the wavelength range 250–350 nm) and emit dominantly in the near-UV and blue part of the spectrum ($\lambda \sim 350$–500 nm). Many polyaromatic hydrocarbons (PAHs, including pyrene and fluoranthene that are mentioned in Table 1) have been found in the Murchison meteorite and are thus examples of abiotic extraterrestrial organic compounds (Pering and Ponnamperuma, 1971). Inorganic examples include the blue–violet fluorescence of plagioclases (activated by Eu^{2+}, Gorobets and Rogojine, 2002, p. 45; Robbins, 1994, p. 126) and opal/chalcedony green fluorescence caused by traces of UO_2^{2+} (Gorobets and Rogojine, 2002; Warren et al., 1995; see Milliken et al., 2008 and Squyres et al., 2008 on opaline silica deposits on Mars). In general, increasing activator concentration up to a specific level brightens the luminescence. However, above this characteristic content of activators the luminescence fades away, a behavior referred to as concentration quenching (Warren et al., 1994; Gaft et al., 2005). Often, luminescence requires not only an activator, but also a co-activator (also called sensitizer) that absorbs incident UV photons and transfers the energy efficiently to the activator ions. The best-studied example of this phenomenon is the red fluorescence of calcite that is activated by Mn^{2+} and co-activated by Pb^{2+} (or in some cases Ce^{3+}, Robbins, 1994, p. 203; Sidike et al., 2006).

It is reasonable to ask whether luminescent material can be expected on the surface of Mars since one of the best luminescence quenchers (triggers for non-radiative decay) is Fe^{2+} (Gaft et al., 2005; Warren et al., 1995). As a result, olivine ($(Mg,Fe)_2SiO_4$) is generally non-luminescent, although pure (strictly iron-free) forsterite (Mg_2SiO_4) sometimes does exhibit VIS luminescence (Gorobets and Rogojine, 2002, p. 44). The trivalent iron (Fe^{3+}) also acts as a luminescence quencher (disregarding a few exceptions such as orthoclases in metasomatites, Gorobets and Rogojine, 2002, p. 45; Warren et al., 1995, p. 154). More importantly, Ni^{2+} quenches luminescence as efficiently as Fe^{2+}. Since (average) Martian soils contain almost 10 wt% Fe^{2+} and a few wt% of Fe^{3+} (Gellert et al., 2006, Morris et al., 2006), and since the concentration of Ni (possibly in the form of Ni^{2+}) is enhanced in bright Martian soils ($\sim$650 ppm at the Gusev landing site, Yen et al., 2005), chances to detect luminescent materials on Mars are slim. In summary, the luminescence of a given mineral depends critically on the specific assemblage of trace elements (activator/co-activator ions and the host composition) implying that luminescence is not a reliable tool for identification of minerals. However, the occurrence of luminescent material on Mars would be a valuable geochemical marker for certain trace elements and associated mineral/organic phases.

The fixed-focus OM instrument has been described elsewhere (Hecht et al., 2008 and Goetz et al., 2010a). Several sets of sample substrates mounted on a sample wheel (Hecht et al., 2008) received material that was scooped up from a workspace adjacent to the PHX lander. Each substrate was a 3 mm diameter circular plane disk. Each set included five varieties of substrates: (1) "sticky" silicone, (2) an empty well or "microbucket", (3) a textured silicon-"nano-bucket", (4) a substrate containing a weak magnet, and (5) a substrate with a strong magnet. Soil particles stick to these substrates either by adhesive (sticky silicone or nano-bucket) or magnetic forces (weak or strong magnet). The design of the magnetic substrates and their magnetic interaction with different Mars analog soils has been described by Leer et al. (2008). During image exposure the soil material was illuminated by one or more of a ring of 12 Light Emitting Diodes (LEDs), 3 each of red, green, blue (RGB), and near-UV (Fig. 1). Color micrographs of soils were generated by combining monochrome images acquired separately with red, green, and blue illumination. The typical RGB exposure utilized 2 LEDs of each color for $\sim$1 s each. The images were also corrected for small intensity changes in the blue, green and red LEDs over the course of 100 sols (+4.1%, +2.0%, and −8.7%, respectively; Goetz et al., 2010a).

For most samples, a long-exposure image (typically 31 s) was also acquired under illumination by 3 UV LEDs ($\lambda = 375$ nm). Since the MECA box (Microscopy, Electrochemistry and Conductivity Analyzer, Hecht et al., 2008) containing the OM is not completely light-tight, the long exposure used for the UV-illuminated images required acquisition of a "dark image" with the same exposure time. All UV-illuminated images discussed here are therefore dark-subtracted and are referred to as "UV–D." The differencing also reduces the effect of warm pixels and removes the common pedestal value (bias). The lower signal-to-noise ratio of these

Fig. 1. Front side of the OM. Three clusters (#1, #2, #3) of Light Emitting Diodes (LEDs) obliquely illuminate the target material. The distance from the end of the LEDs to the target is in the range 25–30 mm (Hecht et al., 2008; Goetz et al., 2010a). Each LED cluster is composed of a red (incidence angle $i \sim 30°$), blue ($i \sim 30°$), green ($i \sim 37°$), and UV ($i \sim 37°$) LED. The UV LEDs (Nichia NSHU590E, marked in the figure) are covered by a circular UG-11 Schott filter (1 mm thick) on a titanium alloy holder. The circular aperture in the lower part of the image is centered on the optical axis of the instrument and allows a partial view of the lens system. (From Goetz et al., 2010a). (For interpretation of the references to colour in this figure legend, the reader is referred to the web version of this article.)

Table 1
Luminescence of selected polycyclic aromatic molecules, sorted according to increasing CAR value or wavelength of fluorescent emission. PAH stands for polyaromatic hydrocarbon. CAR is the number of Condensed Aromatic Rings. A related table on fluorescent biomolecules in modern organisms can be found in Smith et al. (2012).

Molecule	Structure	Excitation	Emission	Reference
Tryptophane	Amino acid, CAR=2, N-heterocyclic	$\lambda < 300$ nm	λ=320–400 nm (fluoresecence), λ=400–500 nm (phosphorescence)	Figure 12 in Gorobets and Rogojine (2002).
Fluoranthene	PAH, CAR=4, homocyclic	λ=200–350 nm	λ=350–540 nm	
Pyrene	PAH, CAR=4, homocyclic	λ=220–350 nm	λ=360–450 nm	Figure 1 in Beltran et al. (1998).
Benzo[a]pyrene (BaP)	PAH, CAR=5, homocyclic	λ=220–350 nm	λ=390–470 nm	Osborne and Crosby (1987), p. 295 (BaP).

long-exposure difference images (as compared to the VIS images) has important implications for image analysis. It should also be noted that the need for 31 s UV-illuminated exposures was not anticipated prior to launch, and therefore all relevant calibration was performed in situ during the mission on the surface of Mars.

Following the convention of Goetz et al. (2010a), RGB color images are referred to by sol number and the last four digits of the spacecraft clock time of the red image. UV images (as well as dark-subtracted UV images) are referred to by the corresponding parameters of the UV image.

2. LED emission spectra

Fig. 2a shows the biconical lighting and viewing geometry for the OM. Light emitted by the LEDs is partly absorbed and partly backscattered by the soil sample on the substrate, then transmitted through a lens system and a Schott GG420 filter prior to detection by the CCD (Charge Coupled Device). Fig. 2b and c shows the emission spectra of the LEDs (left ordinate in Fig. 2b and c) compared to the transmission spectrum of the filter and the responsivity of the CCD (right ordinate in Fig. 2b). Reference LED emission spectra were acquired in the laboratory with an Ocean Optics spectrometer, using short exposures to determine the shape of the main emission band (10–100 ms, depending on LED type) and long exposures (3000 ms) to identify weak out-of-band leakage. The UV LED main emission peak is centered at 375 nm and a broad, weak secondary peak was found at ~700 nm (Hecht et al., 2008). The latter emission will be referred to as the NIR peak, although its central wavelength is at the conventional boundary between the visible (VIS) and NIR spectral regions. The CCD detection system should be unable to detect reflected UV

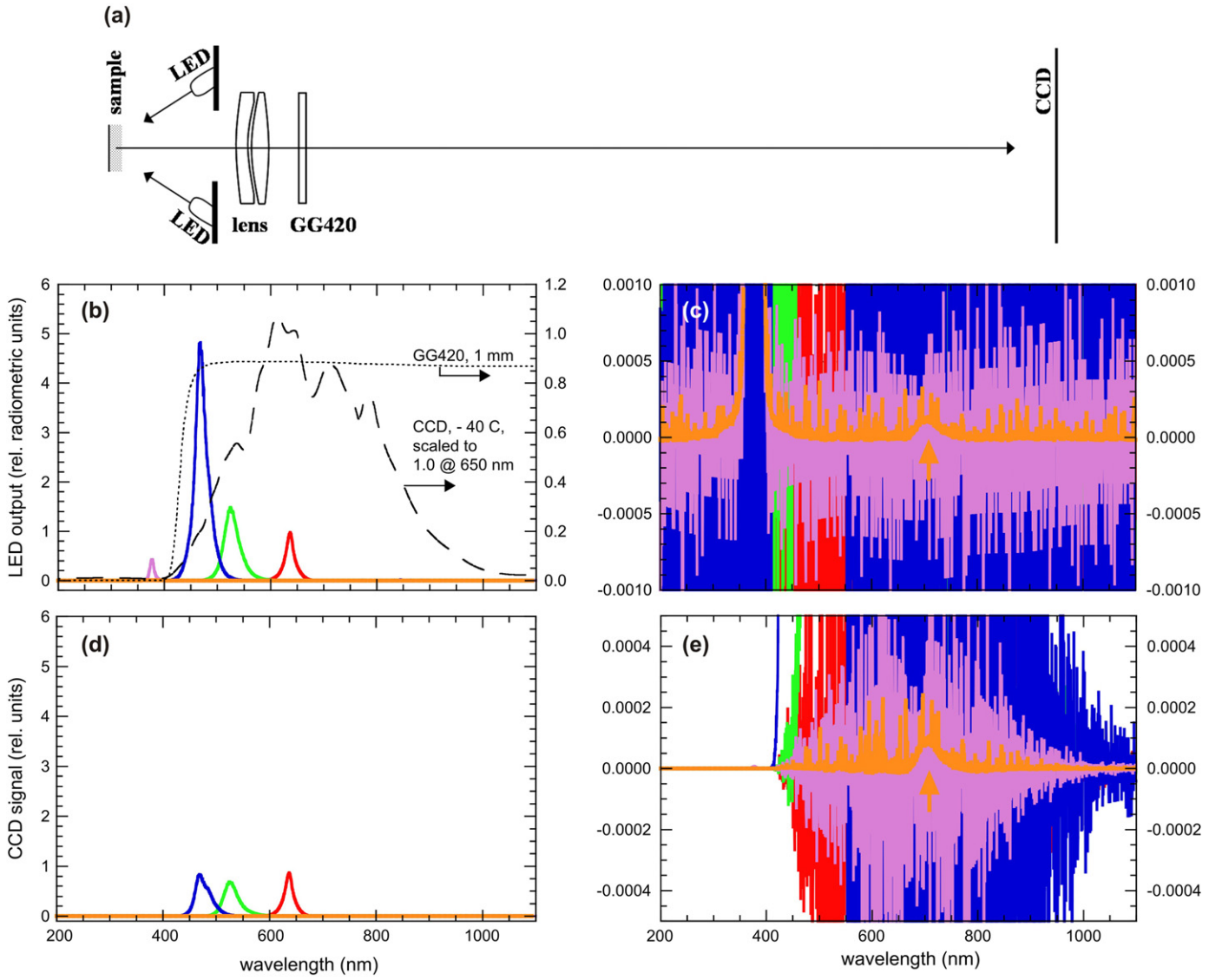

Fig. 2. (a) Major components of the OM and optical path during imaging. The drawing is roughly to scale (except exaggerated sample thickness). The nominal distance from substrate/sample (at working distance) to CCD is about 17 cm. (b) LED spectra in relative radiometric units (proportional to photon flux, left ordinate). Transmission of the Schott filter GG420 and the CCD responsivity (arbitrarily scaled to 1.0 at 650 nm). (c) Zoom of (b), but without filter transmission and CCD responsivity. (d) CCD signal as product of LED output (see b), GG420 transmission, and CCD responsivity. (e) Zoom of (d). Color code for spectra: RED=red LED, GREEN=green LED, BLUE=blue LED, PINK=UV LED spectrum acquired with short exposure duration (25 ms), OCHER=UV LED spectrum acquired with long exposure duration (3000 ms). The UV LED has an out-of-band emission peak at around 700 nm (arrow in c and e). All spectra are in coherent relative units. Thus, when multiplying e.g. the blue LED output with the GG420 transmission and the CCD responsivity (as plotted in b), we get the (expected) spectrally resolved CCD signal [DN ms^{-1} nm^{-1}] for the white calibration target when illuminated by 2 blue LEDs. When integrating that latter spectrum over all wavelengths, we get the signal of the flight model OM in [DN/ms], as measured for the white calibration target with 2 illuminating blue LEDs (cluster #1 and #2, Fig. 1) on sol 4. (For interpretation of the references to colour in this figure legend, the reader is referred to the web version of this article.)

radiation (360–390 nm) due to absorption by the GG420 filter and negligible CCD response in that spectral range (Fig. 2b,d and e). Thus the CCD signal detected during illumination by the UV LEDs is caused either by UV-excited luminescence of the sample, or by NIR light reflected off the sample. The difficulty lies in the separation of these two effects.

Fig. 3 shows two UV-illuminated images, acquired on PHX sols 004 and 057, of the UV calibration target used to assess the stability of the UV LEDs. During acquisition of these images the CCD temperature changed by less than 0.1 K and was about 3 K higher on sol 004 ($T\sim$250.04 K) than on sol 057 ($T\sim$247.05 K). The images indicate a small decrease in UV signal from 1.086 to 1.037 DN/ms, corresponding to about 5%. The radiant output of the Nichia UV LED (NSHU590E) is known to decrease by $\sim$0.9%/K over the temperature range 240–270 K. Assuming the CCD temperature is diagnostic of the LED temperature (which was not directly measured), the drop in temperature explains most of the signal decrease. The remainder may be due to the deposition of a thin dust veil (invisible in OM images) on the UV calibration target over the course of 53 sols. The decrease in signal is not thought to have been caused by degradation of the luminescent material (BAM, Hecht et al., 2008), which is chemically stable.

Fig. 4 illustrates how images of the UV calibration target may be used to infer an order of magnitude for the luminescence Quantum Efficiency (QE) of UV irradiated soil material. The convolution of the camera sensitivity (the product of CCD responsivity and filter transmission) with different model emission spectra (full widths at half maximum (FWHM)=25, 50, or 75 nm) should be proportional to the CCD signal that can be expected as a function of the wavelength (taken at the center wavelength of luminescent emission). These convolutions were scaled such that they represent the actual CCD signal that would be measured if the irradiated target material had a luminescence QE of 100%. The BAM material used for the UV calibration target has an emission spectrum centered at $\lambda\sim$453 nm with FWHM$\sim$50 nm, and its luminescence QE is estimated to be of the order of 40%. When UV-irradiated it generates a CCD signal of$\sim$1 DN/ms (Fig. 3). As a result, all convolutions are scaled to 2.5 DN/ms at λ=453 nm to represent a corresponding luminescence QE of 100% (Fig. 4). Thus, whenever we wish to convert a measured CCD signal caused by UV-excited luminescence into a QE we can assume a bell-shaped emission spectrum (with given center wavelength and FWHM) and read the CCD signal (in DN/ms) expected for QE=100% from Fig. 4 (left ordinate). The ratio of the measured CCD signal to the latter one will provide the luminescence QE of the investigated soil.

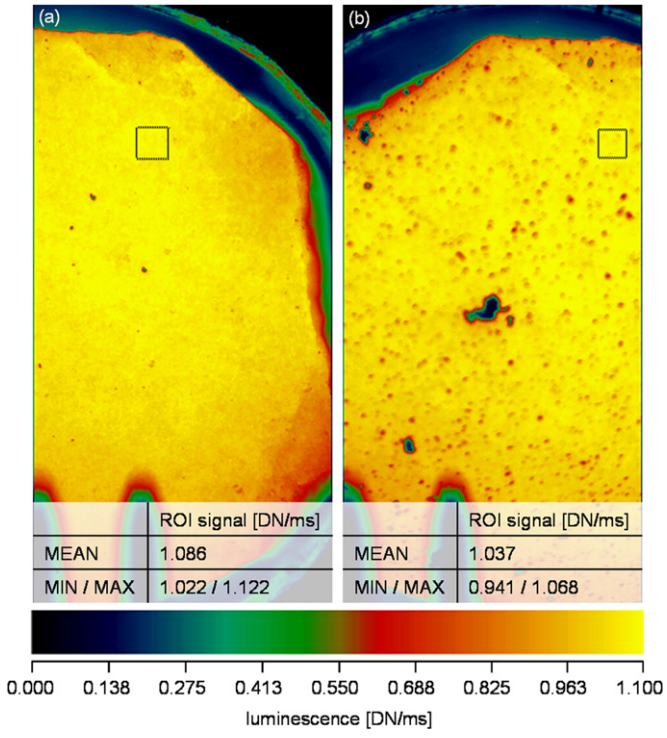

Fig. 3. Images of the UV calibration target (BAM C422): (a) sol 004, #5740, T(CCD)=249.9 K and (b) sol 057, #3377, T(CCD)=247.0 K. The small rectangles near the top of the images specify two ROIs (a: 716 pixels, b: 564 pixels) that are located close to each other on the UV calibration target and – relying on visual inspection – should be a fairly clean area in the sol-057 image. The BAM ceramic material (Zych et al., 2004; Hecht et al., 2008) has high quantum efficiency (of the order of 40%) for UV-to-VIS luminescence. Therefore the UV signals (corresponding to these ROIs, $\sim$1 DN/ms, see tables in a and b) are about 1000 times larger than those observed during irradiation of PHX soil samples ($\sim$0.001 DN/ms, see Fig. 6). Other clean ROIs (not shown here) gave similar results. The observed decrease in signal from 1.086 (sol 004) to 1.037 DN/ms (sol 057) is believed to be due to a lower temperature of the UV LEDs and to the continuous dust contamination of the UV calibration target, rather than to a change in radiant output of the UV LEDs.

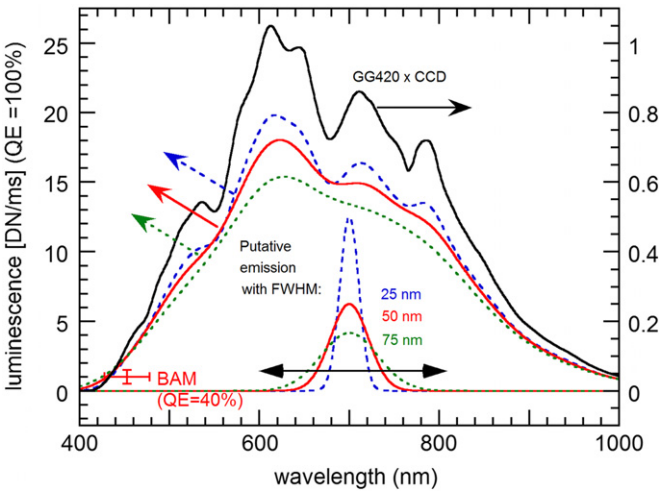

Fig. 4. Dependence of luminescent emission [DN/ms] on wavelength for a QE=100%. The right ordinate refers to the product (expressed in arbitrary units) of filter transmission (GG420, Fig. 2b) and CCD responsivity (Fig. 2b). The right ordinate also refers to three Gaussian-type model spectra of luminescent emission (normalized to the same area). The three bell curves have Full Widths at Half Maximum (FWHM) of, respectively, 25, 50, and 75 nm. A bell curve with FWHM=50 nm and centered at λ=453 nm is a good fit to the BAM luminescence spectrum (see Figure 29 in Hecht et al., 2008). The left ordinate refers to the convolution of the products (in DN/ms) of filter transmission and CCD responsivity with each of the three model spectra whose center wavelength is moved across the spectral region 400–1000 nm, as indicated by the black double arrow. These convolutions (drawn, respectively, with dashed blue, solid red, or dotted green lines corresponding to the respective model spectra) have been scaled to 2.5 at λ=453 nm. This scaling is dictated by the observed CCD signal ($\sim$1 DN/ms, Fig. 3) from BAM, whose luminescence QE is estimated to be 40% (the red cross marks BAM). (For interpretation of the references to colour in this figure legend, the reader is referred to the web version of this article.)

The QE derived in this way is essentially the ratio of emitted VIS photons to incident UV photons. It is *not* the ratio of emitted VIS photons to *absorbed* UV photons. Thus its definition deviates from the one often used in solid state physics. In particular, the QE as derived here is subject to the following uncertainties: (1) we assume that the actual emission spectrum can be described by a single bell-shaped curve. In practice, multiple peaks of different intensities and center wavelengths may be more likely. (2) The light scattering properties of the soil particles are assumed to be similar to those of the BAM pellet used as the UV calibration target. However, these light scattering properties (in particular, the angular profile of radiation emitted into the backward

hemisphere, towards the CCD) depend on the physical properties of the bulk material, including the packing density, size, shape, and albedo of the individual particles. Thus, for the extremely weak luminescence under study, we do not expect better than an order of magnitude accuracy of the QE derived by comparison to the UV calibration target.

3. Analysis

3.1. UV–D difference signal

UV and D data acquired over the course of the PHX mission are summarized in Table 2. Fig. 5 plots the mean UV and D signals of soil/dust areas versus sol number. It can be seen that the UV signal is always slightly higher than the D signal. All D and UV images represent 31-sec exposures acquired with UV-LEDs switched off and on, respectively. The D image documents the small amount of stray light inside the MECA box. The UV image contains the D signal and an additional signal due to illumination of the target by three UV LEDs. Overall, UV and D signals decrease after sol 73 ($L_S \sim 110^\circ$) as the season progresses further into northern-hemisphere summer (sol 30–208, the mission ended around sol 148). Fig. 5 also plots the CCD and atmospheric temperatures, the latter measured at the top of the meteorological mast, ~1 m above the lander deck, and averaged over 512 s long time intervals that encompass the acquisition of the relevant UV and D images. The correlation between UV and D signals on the one hand and CCD and atmospheric temperatures on the other hand may suggest a causal link between both types of data. In particular the UV and D peak around sol 105–110 should not show up in the temperature plots, if the UV and D signals were fully controlled by stray light. However, according to pre-flight characterization data the CCD signal should be fairly independent of temperature (see Figure 13 in Keller et al., 2008). Thus the overall dependence of the UV and D signals on sol number remains unclear.

Fig. 6 plots the red (R), green (G), and blue (B) signal (left ordinate) as well as the UV–D difference signal (right ordinate) versus sol number. The UV–D signal was typically in the range 0.0005–0.0010 DN/ms throughout the mission and depends on the sol number in a similar way as the UV and D signals plotted in Fig. 5.

Fig. 7a shows the standard deviation of UV–D difference pixels within soil/dust covered areas in each image (sols 20 through 130 as in Figs. 5 and 6). From out-of-focus UV/D images (not further discussed here) the combined OM read noise and Poisson shot noise is inferred to be of the order of 0.0001 DN/ms rms, which we take as a lower bound to the observed standard deviations (0.0001 to 0.001 DN/ms rms, Fig. 7a).

Fig. 7b and c illustrate the effect of compression and show that the standard deviation of the same area (ROI #0 in sol-99 images) is ~0.0003 and ~0.0004 DN/ms rms for lossless compression (Rice algorithm, Healy, 1998) and JPEG compression (3 bits per pixel), respectively (see arrows in Fig. 7a). In general such standard deviations should be controlled by particle diversity, sample topography and image compression. However, Fig. 7b and c shows that they are significantly affected by data handling (compression) and do not represent a reliable measure for particle diversity. Only Rice compressed images have sufficient quality, but such images were only downloaded a few times during the mission.

The question arises how the UV–D difference signal can be used to assess luminescence of Martian soil. Given the instrumental and data constraints as described so far we can try to quantify luminescence in two ways: (1) Knowing that part of the UV–D signal (or even the entire signal) is caused by reflection of the NIR radiation from the UV LED, we can consider UV–D to be a crude upper bound to luminescence of Martian soil (Section 3.2) (2) Assuming that Martian soil is composed of a non-luminescent matrix and some luminescent particles we can search for the latter type of particles and estimate their luminescence (relative to the matrix, Section 3.3).

3.2. Upper bound to luminescence of bulk soil

Ignoring the NIR reflectance contribution, the UV–D signal in Fig. 6 (~0.001 DN/ms) corresponds to a luminescence QE of 0.040% and 0.006% for, respectively, bluish (~2.5 DN/ms for QE=100%, Fig. 4) and reddish emission (~18 DN/ms for QE=100%, Fig. 4). Thus we take QE=0.04% as a crude upper bound for the overall luminescence of bulk PHX soil. This value is slightly higher than our earlier upper bound (0.01%, Goetz et al., 2010b). The inferred QE refers to "bulk soil", i.e. a macroscopic sample that is large enough to contain all common types of soil particles with representative abundance. Individual particles or minor mineral phases (Section 3.3) could (at least theoretically) have a larger QE. As emphasized in Section 2 the term "QE" (as used here) assumes Martian soil and the BAM pellet to have similar light scattering properties.

3.3. Search for luminescent soil particles

The remainder of this paper focuses on one particular image cube acquired on sol 99, i.e. #1020 (R), #1050 (G), #1080 (B), #1300 (D), and #1360 (UV). This image cube (highlighted earlier in Section 3.1) shows large amounts of Martian soil in all image types (R, G, B, D, and UV, Figs. 8 and 9) and, in addition, it contains the D and UV frames with lossless (Rice) compression. The Rice compression provides (more or less) true luminosity maps that should be devoid of major artifacts (disregarding hot pixels).

Fig. 8 shows an approximate true-color mosaic of the nano-bucket substrate OM43 and the corresponding UV–D image (returned from Mars with lossless compression). The design of the nano-bucket substrate is described in the Supplemental Online Material (SOM). Fig. 9 shows the right, soil-rich part of OM43 before and after soil delivery. A Region of Interest (referred to as ROI #0) encompassing the soil-covered regions has been manually defined and is outlined in (b). The average CCD signals of ROI #0 (denoted mean(R), mean(G), mean(B), mean(UV–D)) are listed in Table 3.

3.3.1. Hot pixels

All conclusions in this paper are based on UV–D difference images. Differencing two images of the same scene and with similar signal level should in principle remove hot pixels. However, because hot pixels may not have a reliable linear responsivity to incident light, they are discarded in this analysis.

Hot pixels were identified as follows: The entire frame (or the relevant area, such as ROI #0, see Fig. 9b) was studied pixel by pixel. For each individual pixel (except for border pixels) the median value of that pixel and its eight nearest neighbors was determined. If the value of the individual pixel exceeded that median value by some factor, referred to as threshold, the pixel was flagged to be a "warm" pixel. This procedure was separately applied to five Rice compressed 31-sec dark images that were acquired during the mission: sol 76, #9953 (nano-bucket, set 07); sol 76, #9830 (nano-bucket, set 07); sol 76, #9706 (nano-bucket, set 07); sol 99, #1547 (nano-bucket, set 06); sol 99, #1300 (nano-bucket, set 06). The last mentioned dark image includes ROI #0. The intersection of "warm" pixels that are common in all 5 frames

Table 2
OM images (UV, Dark, R, G, B) analyzed in the present work (see Figs. 5–7). Only soil-covered areas in these images were analyzed. UV/D images from sol 110 and from later sols were downloaded as 2×2 binned frames (128×256 pixels) in order to reduce data volume. In 2×2 binned frames each square of 2×2 pixels is replaced by a single pixel with pixel value equal to the sum of the original four pixels. The columns are numbered on top of the table. Column #2 provides the last 4 digits of the spacecraft clock time (used as image ID, see Section 1) for acquisition of dark (D), UV, red (R), green (G), and blue (B) images. Column #3: Compression in bits per pixel (bpp). "Rice" stands for lossless compression (Healy, 1998). Column #4: Encoder value for sample wheel translation (motion along the OM optical axis). Column #5: Encoder value for sample wheel rotation (motion perpendicular to the OM optical axis). Column #6: Substrate set number. Column #7: Unique substrate ID (as given in Fig. 3 in Hecht et al. (2008)). Column #8: Substrate type (Weak Magnet (WM), Strong Magnet (SM), nanobucket (nano), microbucket (micro)) with specification of subregion on that substrate (left (le), middle (mi), right (ri)). The nanobucket is also referred to as "textured substrate". See the Supplemental Online Material to the present paper and Hecht et al. (2008) for further information on these substrates. Column #9: Name of soil sample (see Table 1 in Goetz et al. (2010a)). Beyond the samples mentioned here one more sample was delivered by the robotic arm to the OM (Wicked Witch, substrate set #7). However, no coherent set of Wicked Witch images (D, UV, R, G, B) was acquired.

[#1] Sol	[#2] Image id	[#3] Bpp	[#4] Trans	[#5] Rot	[#6] Substrate	[#7]	[#8]	[#9] Soil sample
					Set #	ID	Type	
21	D: 7009, UV: 7070, R: 6664, G: 6694, B: 6724	3	49071	20670	2	OM 7	WM (le)	Mama Bear
21	D: 6884, UV: 6945, R: 6572, G: 6602, B: 6632	3	49071	20734	2	OM 7	WM (mi)	Mama Bear
31	D: 4732, UV: 4793, R: 4581, G: 4514, B: 4543	6	48611	18723	1	OM 1	WM (mi)	Rosy Red
33	D: 4275, UV: 4335, R: 4125, G: 4155, B: 4184	6	48511	20056	1	OM 5	SM (mi)	Rosy Red
44	D: 1751, UV: 1812, R: 1565, G: 1595, B: 1625	6	48911	17411	10	OM 69	SM (mi)	Sorceress
44	D: 0652, UV: 0712, R: 0466, G: 0496, B: 0526	6	49111	16077	10	OM 65	WM (mi)	Sorceress
73	D: 9080, UV: 9140, R: 8676, G: 8707, B: 8737	12	49211	13347	8	OM 57	SM (le)	Mother Goose
73	D: 8956, UV: 9017, R: 8585, G: 8615, B: 8644	12	49211	13411	8	OM 57	SM (mi)	Mother Goose
73	D: 8830, UV: 8892, R: 8493, G: 8523, B: 8552	12	49211	13475	8	OM 57	SM (ri)	Mother Goose
73	D: 0000, UV: 0061, R: 9603, G: 9633, B: 9662	12	49111	12013	8	OM 53	WM (le)	Mother Goose
73	D: 9877, UV: 9937, R: 9511, G: 9541, B: 9571	12	49111	12077	8	OM 53	WM (mi)	Mother Goose
73	D: 9753, UV: 9814, R: 9419, G: 9449, B: 9479	12	49111	12141	8	OM 53	WM (ri)	Mother Goose
99	D: 2353, UV: 2413, R: 2137, G: 2167, B: 2196	12	48311	8859	6	OM 43–44	Interstice (le)	Golden Key
99	D: 2657, UV: 2717, R: 2137, G: 2167, B: 2196	3	48311	8859	6	OM 43–44	Interstice (le)	Golden Key
99	D: 2230, UV: 2290, R: 2045, G: 2075, B: 2105	12	48311	8923	6	OM 43–44	Interstice (ri)	Golden Key
99	D: 2533, UV: 2594, R: 2045, G: 2075, B: 2105	3	48311	8923	6	OM 43–44	Interstice (ri)	Golden Key
99	D: 1547, UV: 1607, R: 1206, G: 1236, B: 1265	Rice	48311	8661	6	OM 43	Nano (le)	Golden Key
99	D: 1796, UV: 1856, R: 1113, G: 1144, B: 1174	3	48311	8725	6	OM 43	Nano (mi)	Golden Key
99	D: 1423, UV: 1484, R: 1113, G: 1144, B: 1174	Rice	48311	8725	6	OM 43	Nano (mi)	Golden Key
99	D: 1673, UV: 1733, R: 1020, G: 1050, B: 1080	3	48311	8789	6	OM 43	Nano (ri)	Golden Key
99	D: 1300, UV: 1360, R: 1020, G: 1050, B: 1080	Rice	48311	8789	6	OM 43	Nano (ri)	Golden Key
105	D: 8647, UV: 8708, R: 8958, G: 8988, B: 9018	12	48311	7347	5	OM 39	SM (le)	Pre delivery of Golden Goose
105	D: 8520, UV: 8582, R: 8866, G: 8896, B: 8926	12	48311	7411	5	OM 39	SM (mi)	Pre delivery of Golden Goose
110	D: 1034, UV: 1096, R: 0689, G: 0719, B: 0749	12	48511	6640	5	OM 37	Nano (le)	Golden Goose
110	D: 0909, UV: 0970, R: 0596, G: 0626, B: 0656	12	48511	6704	5	OM 37	Nano (mi)	Golden Goose
110	D: 0784, UV: 0845, R: 0504, G: 0534, B: 0564	12	48511	6768	5	OM 37	Nano (ri)	Golden Goose
110	D: 1693, UV: 1755, R: 1348, G: 1378, B: 1408	12	48511	6806	5	OM 37	Nano (ri)	Golden Goose
121	D: 2344, UV: 2406, R: 2066, G: 2095, B: 2125	12	48511	5475	4	OM 33	SM (ri)	Pre delivery of Galloping Hessian
121	D: 2471, UV: 2533, R: 2157, G: 2187, B: 2217	12	48511	5411	4	OM 33	SM (mi)	Pre delivery of Galloping Hessian
121	D: 2598, UV: 2660, R: 2249, G: 2279, B: 2309	12	48511	5347	4	OM 33	SM (le)	Pre delivery of Galloping Hessian
121	D: 5281, UV: 5342,	12	48511	4077	4	OM 29	WM (mi)	Pre delivery of Galloping Hessian

Table 2 (*continued*)

[#1] Sol	[#2] Image id	[#3] Bpp	[#4] Trans	[#5] Rot	[#6] Substrate	[#7]	[#8]	[#9] Soil sample
					Set #	ID	Type	
121	R: 4968, G: 4998, B: 5029 D: 5156, UV: 5217, R: 4876, G: 4906, B: 4936	12	48511	4141	4	OM 29	WM (ri)	Pre delivery of Galloping Hessian
130	D: 5949, UV: 6011, R: 5670, G: 5700, B: 5730	12	48611	4973	4	OM 32	Micro (le)	Galloping Hessian
130	D: 6734, UV: 6796, R: 6421, G: 6451, B: 6481	12	48611	4744	4	OM 31	Nano (mi)	Galloping Hessian
130	D: 6608, UV: 6670, R: 6329, G: 6359, B: 6389	12	48611	4807	4	OM 31	Nano (ri)	Galloping Hessian

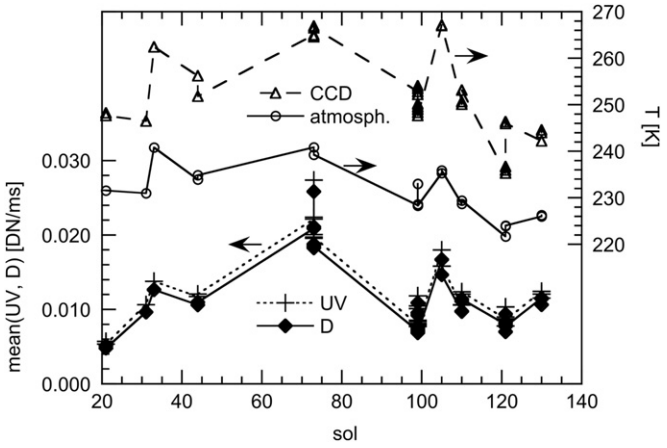

Fig. 5. Evolution of the dark (D) and UV signal (left ordinate) and CCD and atmospheric temperatures (right ordinate) over the course of the mission. Signals and temperatures appear to be correlated. The UV signal must be slightly larger than the dark signal, since the former contains the latter. The curves for both signals are similar in shape to the UV–D difference plotted in Fig. 6. Table 2 specifies the used images. The plotted atmospheric temperatures (Reduced Data Record from PDS archive, http://atmos.pds.nasa.gov/data_and_services/atmospheres_data/Mars/Mars.html) are averages over time intervals of 512 s and have a statistical error (standard deviation) of 1 to 2 K.

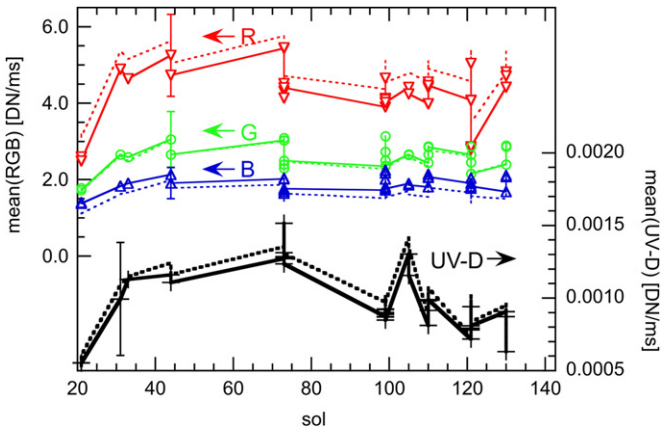

Fig. 6. Evolution of the red, green, and blue signal (left ordinate) and the UV–D difference signal (right ordinate) over the course of the mission. Table 2 specifies the used data. Both ordinates are in units [DN/ms]. Representative error bars are shown at sol 31 (UV–D) and at sol 44 (R, G, B). Solid and dotted lines refer to different Regions Of Interest (ROIs): A large one for soil/dust covered areas (solid lines) and a subregion within the previous ROI for reddish dust (dotted lines). (For interpretation of the references to colour in this figure legend, the reader is referred to the web version of this article.)

are termed "hot" pixels. Fig. 10 plots the number of hot pixels as a function of the choice of threshold.

3.3.2. *Luminescence of selected particles*

We apply two different approaches to search for luminescent particles: (1) Explore the distribution of points in the 4-dimensional image cube (UV–D, R, G, B) and search for clusters that are located in distinct regions of the spectral space. (2) Extract spectral (sub-)populations by an iterative algorithm, plot the mean signal of these populations and search for deviations from a common trend.

The first approach is illustrated in Fig. 11 that shows the UV–D signal of all pixels inside ROI #0 versus B, G, and R, respectively. Pixels exceeding twice the local 3×3 median value have been replaced by that median value. There are 53 such pixels within ROI #0 (Fig. 10). Thus major hot pixels are not displayed in Fig. 11. It can be seen that there is no obvious clustering in the different projections of the multispectral space. In particular there are no populations with anomalously high UV–D values that are clearly detached from the main cluster whose internal structure can be further inspected by the density plots (right column in Fig. 11).

As to the second approach, two alternative methods, referred to as Single Spectral Boundary (SSB) and Double Spectral Boundary (DSB), have been developed to search for luminescence within spectrally selected subsets of pixels.

For the SSB method we calculate the (UV–D) average over pixels that are brighter (or darker) than a given value, the "spectral boundary", in one or several RGB channels. Then we change the spectral boundary and calculate again the (UV–D) average. In that way we define increasingly red (R), green (G), blue (B) or white (W) sub-regions and calculate their (UV–D) average. The initial pixel selection is always a dust/soil-covered area in the image (referred to as ROI #0).

For example, for increasingly reddish material we search for pixels that have decreasing values in the blue channel and increasing values in the red channel. In other words we iteratively decrease the upper B boundary and increase the lower R boundary. The mean UV–D value of all resulting sub-regions is then plotted versus the mean R value. Groups of luminescent pixels are expected to have an anomalously high UV–D signal in these plots.

Fig. 12 illustrates the SSB process by extracting increasingly reddish sub-subsets of pixels/particles from ROI #0 (see Fig. 9b). Initially, the Red Boundary Factor (RBF) and Blue Boundary Factor (BBF) are set to 1.0. Now we search for pixels that are both darker than BBF∗mean(B) and brighter than RBF∗mean(R) (see Table 3) and the (UV–D) average of these pixels is stored. BBF and RBF are then decremented and incremented, respectively, and the procedure is repeated. The green value is not constrained in this

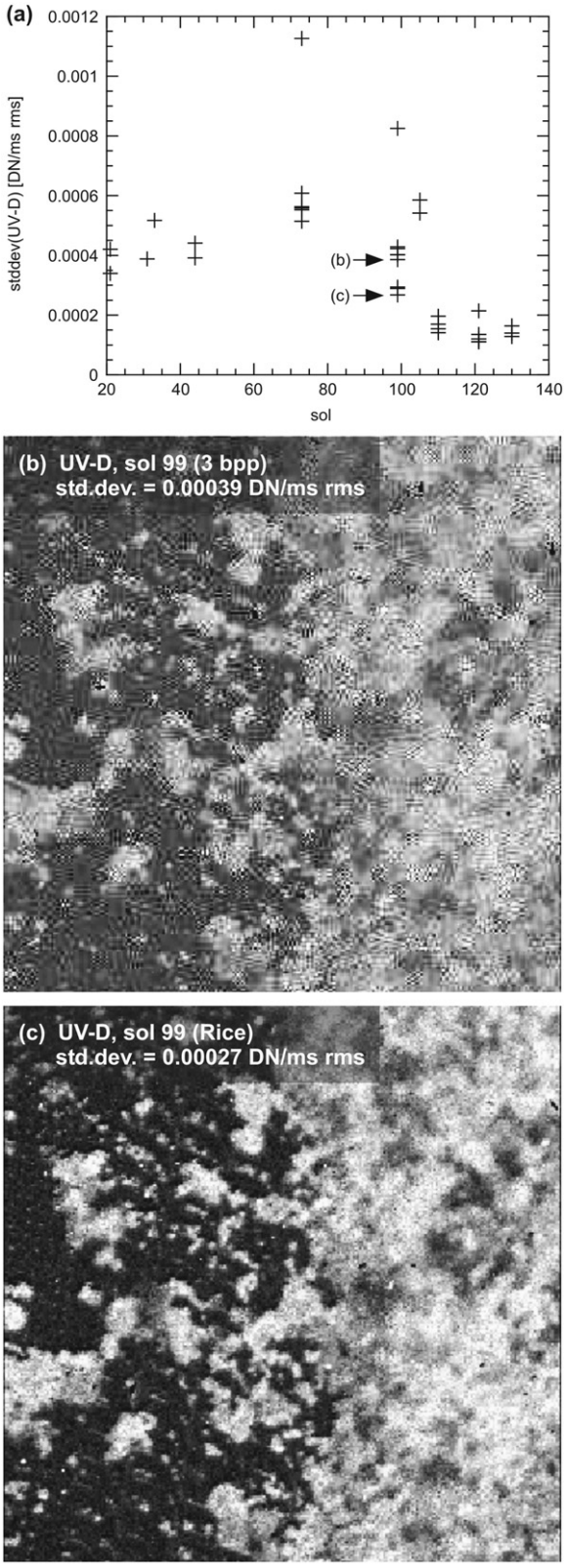

Fig. 7. (a) The standard deviation of UV–D over the course of the mission. On sol 110 and on later sols the standard deviations become very small due to 2×2 binning (Table 2). (b and c) Effect of compression on standard deviation for JPEG compression (3 bits per pixel) and Rice compression (lossless), respectively. (b) and (c) shows half frames of UV–D difference images (central subframes of right part of OM43, see also Fig. 8). Their respective standard deviation is marked by arrows in (a).

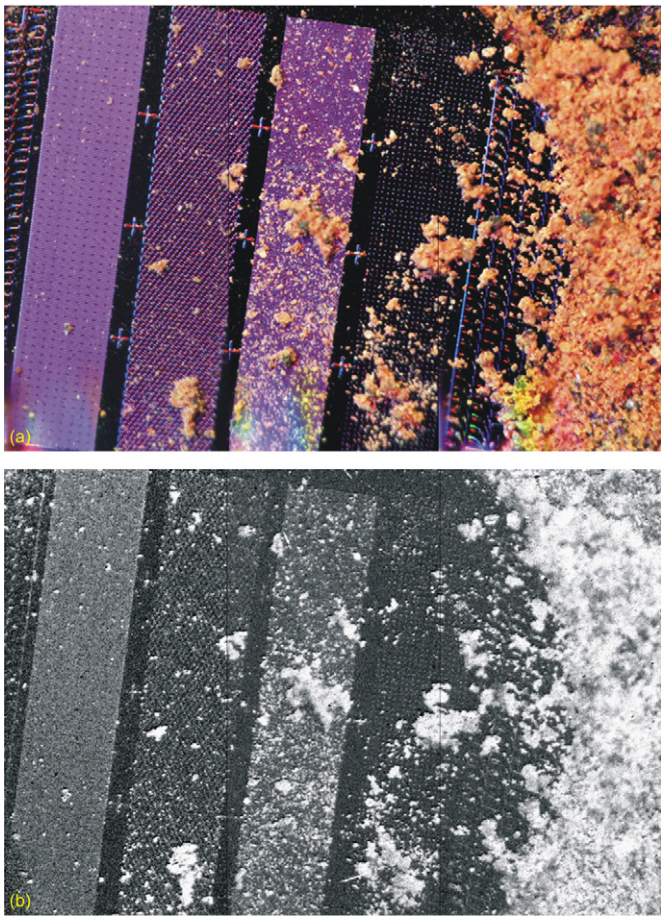

Fig. 8. (a) Mosaics of RGB composite images (sol 99, #1206, #1113, #1020, 6 bits per pixel) and of (b) UV–D difference images (sol 99, #1607, #1484, #1360, Rice) of the nanobucket of set 6 (substrate OM 43 on the sample wheel, Hecht et al., 2008). Most of the soil material does not adhere to the actual target (nanobucket), but to the anodized aluminum surface at the interstice near the right border of the target. Fig. 7c is a subframe of 8b.

example. The way BBF and RBF are varied is indicated in the upper left corner of the plot window in Fig. 12 (a similar legend appears in Fig. 13). Colors in Fig. 12 refer to different thresholds for hot-pixel removal. All thresholds between 1.5 and 2.0 result in the same pixel selection and thus the same UV–D signal. Any threshold in this range attenuates the particularly steep rise in the UV–D signal (black plot symbols in Fig. 12) that we attribute to hot pixels rather than luminescent particles in the soil. We thus choose a threshold of 2.0 to remove "hot CCD pixels" without removing "luminescent pixels". The same threshold value has been used for the scatter and density plots shown in Fig. 11.

The DSB method sorts the spectral properties of pixels into a histogram defined by R, G, or B intervals. The mean UV–D values of the various intervals (bins) are then plotted against the mean R, G or B values. Discontinuities or deviations from smooth (fairly straight) lines can be interpreted as luminescence. Since VIS-NIR reflectance spectra of Martian soil and (terrestrial) Mars analog samples are well-known, such plots can provide constraints on potential luminescence of Martian soil particles or, at least, help identify pixels or particles with unusual spectral properties.

Note that both methods (SSB and DSB) only allow for identification of luminescence, if some (or few) pixels/particles are luminescent in contrast to a non-luminescent soil matrix. These methods will not allow for detection of luminescent particles that are smaller than pixel resolution and uniformly distributed across the entire soil matrix. The advantage of the SSB method lies in the larger number of pixels available in each subset (as compared to DSB). Since the SSB method consists of iterative extraction of a subset of pixels from some ROI, different SSB points in a plot such

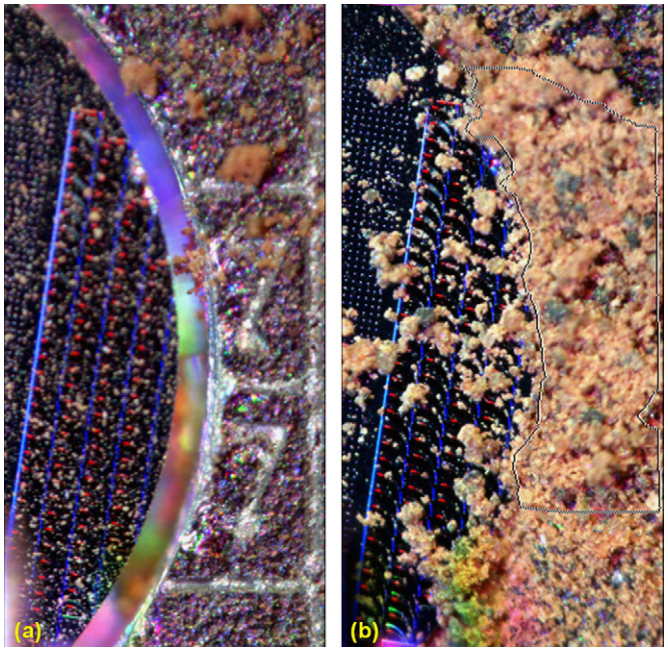

Fig. 9. Nano-bucket (substrate OM43, set 06) before (a) and after (b) sample delivery. The images were acquired on sol 95 (#1239) and sol 99 (#1020), respectively. Figure b also shows the outline of a large Region of Interest (ROI #0, 35960 pixels) that was selected for further analysis in the present paper. The ROI includes most of the (in-focus) soil layer, but excludes the region near the bottom of the image that is discolored due to light scattering by the Atomic Force Microscope (AFM) silicon tips (Hecht et al., 2008).

Table 3
Characteristics of the soil covered region just outside substrate OM43, set 06 (sol 99). The corresponding Region of Interest (referred to as ROI #0, Fig. 9b) contains 35960 pixels (~ 27% of the entire frame). The mean signals are plotted by blue open circles in Fig. 13.

Spectral channel	**Quantity** (as referred to in main text)	**Mean signal [DN/ms]**
UV–D	Mean(UV–D)	0.00084669
R	Mean(R)	4.0084
G	Mean(G)	2.3651
B	Mean(B)	1.7698

as Fig. 12 do not represent independent pixels/particles. Both methods (SSB and DSB) consist of a repetitive search for pixels that satisfy continuously varying spectral conditions. The search is performed as long as ten or more pixels meet these conditions.

Fig. 13 plots UV–D signals versus R, G, and B signal inside the primary ROI (ROI #0, 35960 pixels, see Fig. 9b) by applying the above methods (DSB in a, c, e, and g; SSB in b, d, f, and h). In a and b the color becomes increasingly whitish from left to right, i.e. R, G, and B signals rise simultaneously by an amount equal to 0.01 times the corresponding mean value of ROI#0 (Table 3). In c and d, e and f, and g and h, respectively, the reddish, greenish, and bluish hue of selected particles/pixels increases from left to right. The plots confirm that the UV signal correlates positively with R (a–d) and negatively with G and B (e–h). This is what would be expected from the emission properties of the LEDs (Section 2). As long as only the NIR emission peak of the UV LED contributes to the "UV–D signal", the correlation between mean(UV–D) and mean(R) should be continuous and smoothly rising. In the case of luminescence, when the UV emission peak becomes "active" in addition to the NIR emission peak, the plot for affected pixels/particles would be elevated by an amount that clearly exceeds the

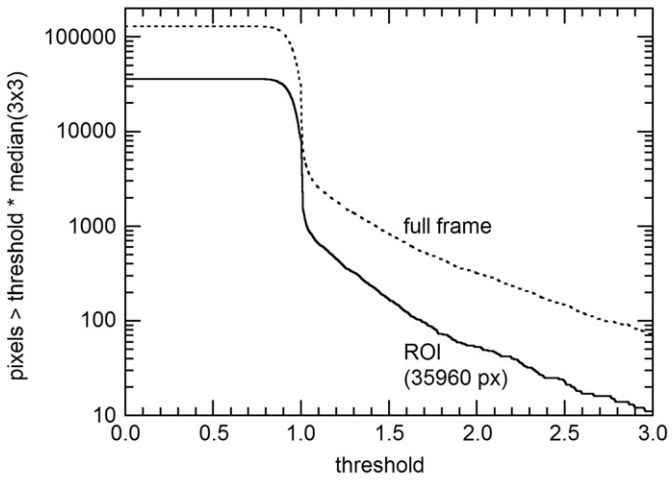

Fig. 10. Number of pixels with elevated DN of the OM CCD (Flight Model). All pixels are counted that have values larger than some factor (here referred to as "threshold") times the local 3 × 3 median value. The solid and dashed lines refer to ROI #0 and the full frame, respectively.

data scatter. In particular, on the right side of each plot where the particles are least absorbing in a given spectral range, their luminescence would clearly show up due to minimum auto-absorption of the emitted luminescent radiation. Potential anomalies are marked by arrows in Fig. 12c and d.

Fig. 13d(SSB) demonstrates that decrementing both B and G while incrementing R (green open triangles) quickly eliminates nearly all pixels. However, when decrementing B and incrementing R, leaving G unconstrained, the curve (black crosses) shows a clear upturn as the mean value of selected pixels in the red channel increases. This may be due to high reflectance of the NIR emission by the most reddish pixels. However, given that the NIR peak (~700 nm) is close in wavelength to the R peak (~634 nm, Fig. 2), this upturn might indeed be indicative of weak luminescence from a few particles, stimulated by the much stronger UV peak of the UV LED emission spectrum.

Such anomalous pixels also show up in Fig. 13c (DSB). While the filled red circle and black cross refer respectively to 24 and 47 pixels, further analysis (SOM, Figure S2) indicates that the elevated mean values are dominated by six pixels with mean(UV–D)~0.0011 to 0.0013 DN/ms.

Subtracting mean(UV–D)~0.00098 DN/ms (Fig. 13c) as possible measure for the background caused by NIR reflectance would leave us with a (presumably reddish) luminescent signal of 1 to 3 10^{-4} DN/ms. The latter signal would correspond to a luminescence QE of typically ~0.001% (assuming that a QE of 100% would generate 18 DN/ms, Fig. 4). However, 6 (out of 35960) pixels is an excessively small pixel fraction (~0.02%) so that the identification of luminescence of the corresponding soil particles remains questionable.

4. Future UV-excited luminescence experiments

Martian soil particles at the PHX landing site were found to be basically non-luminescent when illuminated by UV LEDs (λ~375 nm). Future experiments of similar type and on similar samples will therefore require increasingly sophisticated strategies to elicit a luminescent response, without sacrificing the high spatial resolution that allows investigation of fine (e.g. silt-sized) particles in soils, inclusions in volcanic rocks (phenocrysts, xenolithic inclusions), and the microstructure (facies) of sediments and sedimentary rocks. These strategies might include:

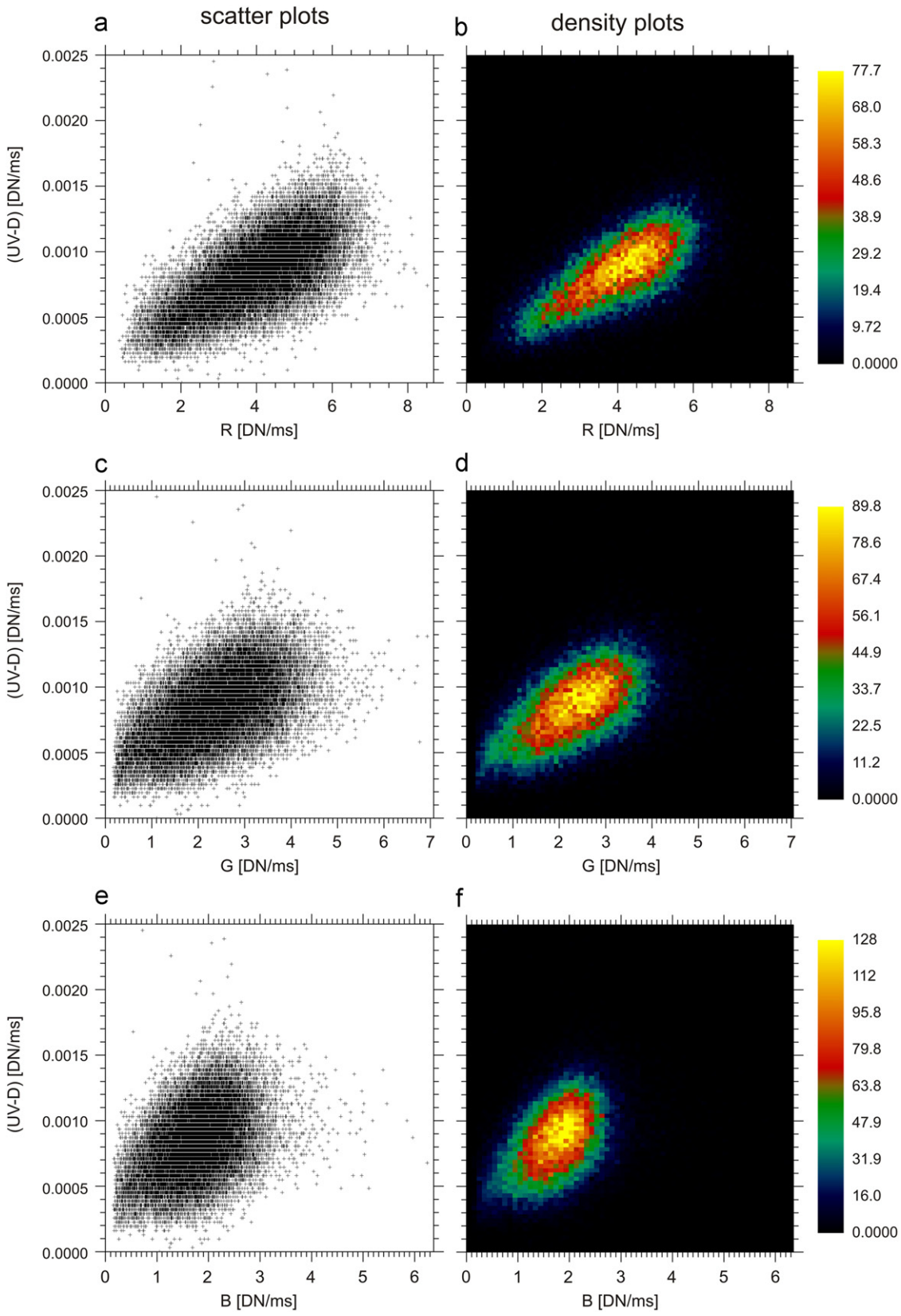

Fig. 11. Scatter and density plots for UV–D (ROI #0, Fig. 9b) versus R (a and b), G (c and d), and B (e and f). The scatter plots (left column) show all 35960 pixels within ROI #0 except 5 randomly distributed pixels UV–D larger than 0.0025 DN/ms. The large majority of pixels appear to belong to one single population. In particular no group of luminescent pixels can be discerned in these plots. The equidistant horizontal stripes in the scatter plots express the quantization of the CCD detector and have a nearest-neighbor spacing of $\Delta y_0 = 3.218$ 10-5 DN/ms ~ 1 DN/31 s. The density plots (right column) complement the scatter plots by displaying the number of data points within a rectangle $\Delta x \cdot \Delta y = \Delta y_0 \cdot$ 0.1 DN/ms.

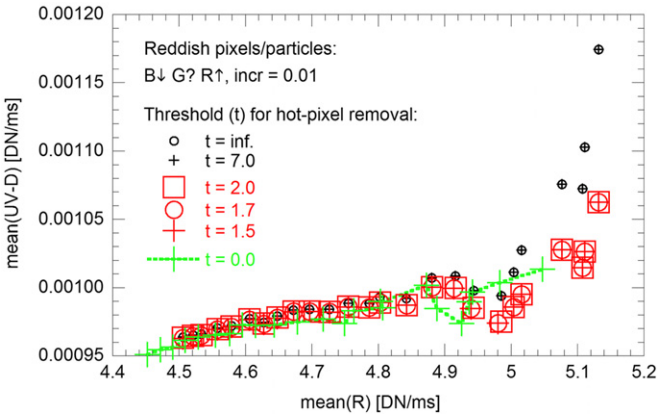

Fig. 12. UV–D signal versus R signal inside ROI #0 (see Fig. 9b). The different points were obtained by extracting increasingly reddish sub-subsets of pixels/particles from ROI #0. In this particular case the blue signal (B) is constrained by a (continuously decreased) upper bound and a (constant) zero lower bound. The lower bound is actually not active, as none of the pixels is equal to zero. Thus the blue pixel selection is effectively controlled by one single bound (the upper one), as indicated by the downward arrow in the legend (B↓). Similarly the red pixel selection is performed by a (continuously increased) lower bound and an "infinite" upper bound, as indicated by an upward arrow (R↑). The green signal is not used for pixel selection, as indicated by the question mark (G?). The step for lowering the blue upper bound or raising the red lower bound is given by the increment parameter (incr=0.01). Red and blue pixel requests are applied simultaneously by an AND logical operator and lead to a selection of increasingly reddish pixels. Different colors of plot symbols refer to different thresholds (denoted by t) for hot-pixel removal. The UV–D signal without hot-pixel correction (small black circles) rises steeply for a red signal larger than 5 DN/ms. This feature persists when applying a hot-pixel correction with a threshold equal to 7 (small black crosses). However, a correction with thresholds in the range 1.5–2.0 does remove a significant fraction of that peak. The remaining peak may be interpreted to be caused by luminescent particles in the PHX soil. Note that thresholds in the range 1.5–2.0 (red plot symbols) have a similar effect on the result. (For interpretation of the references to colour in this figure legend, the reader is referred to the web version of this article.)

(1) Excitation with deep UV ($\lambda \sim$250–300 nm) which is known to stimulate luminescence much more efficiently and in far more types of minerals than near-UV (Warren et al., 1995). This may also apply to candidate organic molecules (see Section 1 and Table 1). Deep UV LEDs are commercially available, but should be configured with an optical filter to reduce VIS leakage. Of course, the use of deep UV LEDs on Mars (or other planetary bodies) requires that a space-qualified product is available.

(2) Reducing stray visible light sources by the use of baffles around the camera body and by night-time operation.

(3) Searching for phosphorescence by delaying the camera shutter until the light source is shut off. The search for phosphorescence can be performed with very high sensitivity as the UV light source that typically has some leakage in the VIS part of the spectrum is switched off during measurement (image acquisition). The experiment can be performed in two ways: (a) Image some homogeneous soil patch after half of that patch was irradiated by UV and compare the DN level in both halves of the image, and/or (b) image some/any soil patch twice, -the second time after prolonged and intense UV irradiation. The images acquired by (a) or (b) are simply "Darks" and may not show morphological features of soil grains or soil topography (depending on the night-time stray light level, see 2). Method (a) has the advantage that analysis is based on one single image. Thus changes in detector sensitivity (e.g. caused by drift in CCD temperature) are ruled out. However, method (a) requires perfect homogeneity (ideal mixing) of the imaged soil patch. Method (b) is based on radiometric comparison of two separate images of the very same soil patch. Thus it requires stability of detector (CCD) parameters and the absence of dust/grain motion (no wind gusts) within the time frame of the experiment. Disregarding these minor constraints any (homogeneous or heterogeneous) soil patch can be investigated by method (b).

(4) Accessing different types of surface material (rocks, soils, and dust). For an arm-mounted imager, a stabilizing device in contact with the sample (contact sensor probe) may be needed to mitigate vibration caused by wind or spacecraft activities. This device should be required to work on both soils and rocks.

(5) Performing spectral analysis of emitted light by using either a color sensitive detector (CCD or CMOS with color microfilters) or a monochrome one configured with a filter wheel.

These strategies are of course tailored to the search for luminescence on the Martian surface, but should work for any other body on which a spacecraft can land (e.g. Moon, asteroids, Titan, etc.). Obviously, strategies referring to atmospheric stray light or wind become irrelevant in the case of airless bodies. The effect of stray light from stars (other than the sun) should not be of any concern, as it can be easily accounted for by the UV–D difference frame.

Strategies (3), (4) and (5) will be utilized in the upcoming Mars Science Laboratory (MSL) mission, which will have the capability to perform a UV illumination experiment using the MAHLI close-up color imager mounted on a turret at the end of the Curiosity rover's robotic arm.

MAHLI's main task is high-resolution color imaging of Martian regolith and rocks. Its UV capability was included on best-efforts, exploratory basis to assist in identification of materials imaged at night. MAHLI utilizes a color CCD with Bayer filter pattern (Edgett et al., 2009) and offers variable focus (and thus variable magnification). Its spatial resolution varies from 14 μm/pixel to poorer resolution at larger distances (Edgett et al., 2009).

During typical operations, the MAHLI will be used to acquire RGB color images of targets illuminated by direct sunlight and/or two independently controlled pairs of white LEDs. However, MAHLI is also able to acquire color images while illuminating the target by a pair of UV LEDs. Thus MAHLI, like the PHX OM, has the potential to detect UV-luminescent materials. The MAHLI color CCD, unlike the monochrome OM CCD, can distinguish blue, green, and red luminescence. Since MAHLI is mounted on a robotic arm, it can image both rocks and soils, though at considerably lower resolution than the Phoenix OM. Differences between MAHLI and OM UV experiments are summarized in Table 4.

MAHLI UV LEDs are similar to those on the OM, emitting in the spectral range 350–390 nm with peak emission ~365 nm (Table 4). During acquisition of UV images, blue, green, and red pixels detect light from target luminescence as well as visible stray light reflected off the target. The stray light consists of VIS leakage from the UV LEDs and/or scattered sky light. Its contribution to the CCD signal reduces considerably the signal-to-noise ratio in the UV–D images. The sky light contribution will be minimized by performing the MAHLI UV experiment at night.

Experience with OM data analysis suggests certain operational strategies for MAHLI that may reduce experimental artifacts: (1) redundant UV and D exposures are helpful to distinguish cosmic ray events from luminescence, and (2) lossless compression of UV and D images avoids errors in UV–D subtraction. The latter will be important, if the putative luminescent soil particles are -as expected- weakly luminescent and small in size (close to the limit of resolution).

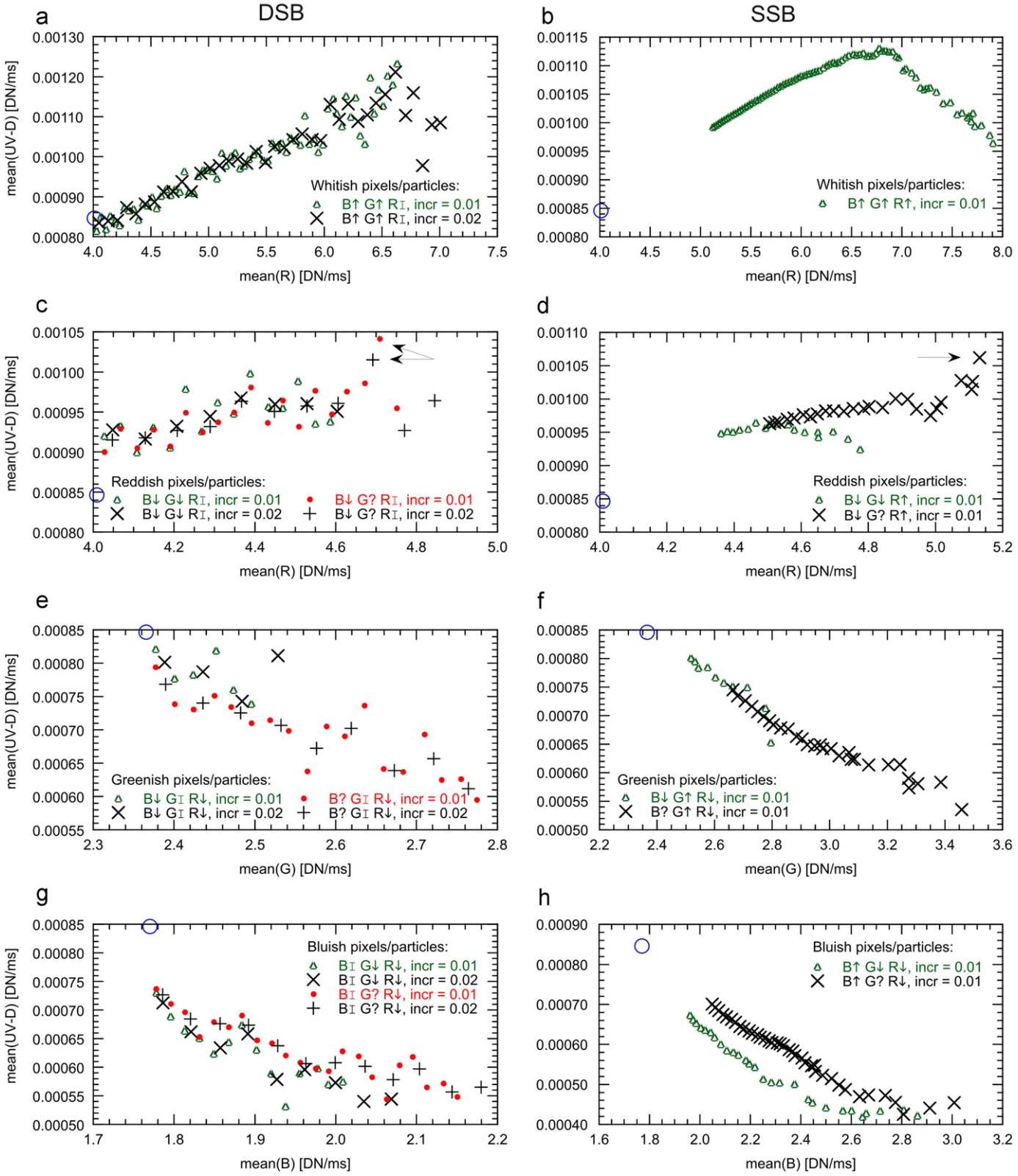

Fig. 13. UV–D signals versus R, G, and B signal inside ROI #0. In all calculations hot pixels were removed with a threshold value equal to 2.0 (see Fig. 12). The single blue open circle represents the mean value over all pixels in the initial ROI (35960 pixels). In each plot the whitish (a and b), reddish (c and d), greenish (e and f), and bluish (g and h) color of selected particles/pixels increases from left to right. Pixels were selected in a systematic way as given in the legend that uses the same symbols as in Fig. 12. Plots in the left (a, c, e, g) and right column (b, d, f, h) use the DSB and SSB method, respectively (see main text). DSB plots refer to independent ROIs, thus each data point represents a subgroup of pixels with no pixel overlap between different points. In the SSB plots we start with a large ROI (large number of pixels) and extract iteratively smaller and smaller subsets of that ROI. Consequently the data scatter is much smaller in SSB plots, as the mean values plotted there are based on a much larger number of pixels. All data plotted here are mean values over at least 10 pixels. Overall these plots confirm that the UV signal correlates positively with R (a–d) and negatively with G and B (e–h). Some pixel selections (ROIs) may be interpreted to contain luminescent pixels/particles (see arrows in c and d), but this remains questionable (see text). (For interpretation of the references to colour in this figure legend, the reader is referred to the web version of this article.)

Table 4
Some characteristics of the MAHLI and OM UV experiments. The parameters of both experiments are quite different. In particular the differences in (1) spectral sensitivity, (2) spatial resolution, and (3) stray light level have major implications for the type of science that can reasonably be returned by these experiments. The data refer to Room Temperature (RT, 25 °C) unless otherwise specified. FWHM (Full Width at Half Maximum) specifies the full (spectral or angular) width of the UV LED light cone at half maximum intensity. LST=Local Solar Time (24 Mars-hour basis).

	UV microscopic experiment	
	OM (PHX)	**MAHLI (MSL)**
Target material	Soils	Soils and rocks
Imaged sample area	1×2 mm (fixed focus)	$\geq$ (17×22 mm) depending on focus
Spatial resolution at sample	4 μm/px	14 μm/px at best (depending on focus)
UV excitation, characteristics of UV light source	$3 \times$ UV LED Nichia NSHU590E, $\lambda_{center}=375$ nm, FWHM=10 nm, Directivity: FWHM$\sim$14° Output power decreasing at lower T: $\sim$0.9%/K in the range 240–270 K	$2 \times$ UV LED Nichia NSHU550B, $\lambda_{center}=365$ nm, FWHM=13 nm, Directivity: FWHM$\sim$100° Output power decreasing at lower T: $\sim$0.3%/K in the range 240–270 K
Detection of reflected/emitted light	Monochrome frame transfer CCD, Loral-Fairchild/Max Planck 256×512 px, sensitive to $\lambda=400$–1000 nm	Interline transfer CCD (Bayer filter), Kodak KAI-2020CM, 1600×1200 px, sensitive to $\lambda=380$–690 nm
VIS stray light level	Minimum stray light (OM in nearly light-tight box)	Martian skylight, depending on LST

Observation of luminescent materials on Mars by the MAHLI might involve a two-step process: (1) First, position the MAHLI for night observing and acquire an image with UV illumination and an associated dark image with same exposure duration (several such image pairs could be acquired with different exposure durations); include a white LED-illuminated image, as well; all images are returned in lossy compressed form but the raw data are stored onboard the instrument. (2) Second, after assessment of the returned UV LED-illuminated and dark images, determine whether a luminescent material was observed and decide whether to (a) acquire additional new data (i.e., the rover would have to return the MAHLI to the previous position) or (b) return the data already acquired, but with lossless compression. There are many operational permutations of this approach that could be used to maximize the science return for cases in which a luminescent material is detected.

Good co-registration between UV, D, and VIS color images will be the key to data analysis and sets narrow constraints to allowable robotic arm vibrations, if any should occur. Such vibrations could be minimized by omitting other spacecraft activities during MAHLI imaging and by choosing a favorable robotic arm joints configuration.

5. Summary and conclusions

PHX optical microscope data were examined for evidence of soil particles exhibiting near-UV-excited luminescence, as indicated by pixels with an anomalously high intensity in UV–D difference frames. This was done over the entire PHX mission (Section 3.1) as well as for a particular (high-quality) data set that was acquired on sol 99 (Sections 3.2–3.3).

The luminescence of PHX soil was inferred to have QE $< 0.04\%$ (Section 3.2). This upper bound is a very conservative one, in the sense that it assumes the total absence of VIS leakage of the UV LEDs. Thus there is good reason to believe that the true upper bound is somewhat lower. In fact, the radiometric properties of very few (anomalous) pixels are consistent with QE$\sim$0.001% (Section 3.3). However, this assertion remains questionable, as these anomalous pixels are not correlated with specific VIS microscopic features.

Overall, no luminescence of PHX soil particles was definitively detected, and it can be firmly concluded that PHX soils do not contain easily resolved (>10 μm) luminescent (inorganic or organic) phases. Note, however, that OM observations were restricted to loose material at the PHX landing site that was scooped up and delivered by the robotic arm to the OM instrument.

The MAHLI instrument on MSL will have a similar UV experiment, though with much lower spatial resolution than the Phoenix OM (Table 4). MAHLI is capable of imaging rock surfaces in a wide range of geologic settings within the rover's field site, and it will be operated at a location on Mars, Gale Crater, for which remote sensing observations suggest there is a very different mineralogy and geologic history relative to the PHX site (Heet et al., 2009; Milliken et al., 2010).

Acknowledgments

This research was supported in part by Deutsches Zentrum für Luft- und Raumfahrt e.V. (DLR) grant 50 QM 0602, the UK Science and Technology Facilities Council, the Wolferman Nägeli Foundation, and NASA/JPL. M.B. Madsen acknowledges support from the Danish Research Agency and from the Lundbeck Foundation. The manuscript was improved by thoughtful comments from Jeffrey R. Johnson, Johns Hopkins University, Applied Physics Laboratory.

Appendix A. Supplementary material

Supplementary data associated with this article can be found in the online version at http://dx.doi.org/10.1016/j.pss.2012.05.002.

References

Beltran, J.L., Ferrer, R., Guiteras, J., 1998. Multivariate calibration of polycyclic aromatic hydrocarbon mixtures from excitation-emission fluorescence spectra. Analytica Chimica Acta 373, 311–319.

Edgett, K.S., Ravine, M.A., Caplinger, M.A., Ghaemi, F.T., Schaffner, J.A., Malin, M.C., Baker, J.M., DiBiase, D.R., Laramee, J., Maki, J.N., Willson, R.G., Bell III, J.F., Cameron, J.F., Dietrich, W.E., Edwards, L.J., Hallet, B., Herkenhoff, K.E., Heydari, E., Kah, L.C., Lemmon, M.T., Minitti, M.E., Olson, T.S., Parker, T.J., Rowland, S.K., Schieber, J., Sullivan, R.J., Sumner, D.Y., Thomas, P.C., and Yingst, R.A., 2009. The Mars Science Laboratory (MSL) Mars Hand Lens Imager (MAHLI) flight Instrument. LPSC XL, #1197.

Gaft, M., Reisfeld, R., Panczer, G., 2005. Modern Luminescence Spectroscopy of Minerals and Materials. Springer, Heidelberg.

Gellert, R., et al., 2006. Alpha Particle X-Ray Spectrometer (APXS): results from Gusev crater and calibration report. Journal of Geophysical Research 111, E02S05, http://dx.doi.org/10.1029/2005JE002555.

Goetz, W., et al., 2010a. Microscopy analysis of soils at the Phoenix landing site, Mars: Classification of soil particles and description of their optical and magnetic properties. Journal of Geophysical Research 115 E00E22 http://dx.doi.org/10.1029/2009JE003437.

Goetz, W., Hecht, M.H., Madsen, M.B., Hviid, S.F., Pike, T., Staufer, U., Leer, K., Elmaarry, M., Keller, H.U., Markiewicz, W.J., 2010b. Spectral properties of soil grains as inferred from images of the optical microscope onboard the Phoenix Mars lander. American Geophysical Union, Fall Meeting 2010, abstract #P53 A-1482, 〈http://adsabs.harvard.edu/abs/2010AGUFM.P53A1482G〉.

Gorobets, B.S., Rogojine, A.A., 2002. Luminescent spectra of minerals. reference-book. Spravochnik, All-Russia Institute of Mineral Resources (VIMS), ISBN 5-901837-05-3 (English edition), Moscow.

Healy, D.J., November 1998. Lossless compression: the Rice alternative to JPEG. In: Fishell, W.G., Andraitis, A.A., Fagan, M.S., Greer, J.D., Norton, M.C. (Eds.), Proceedings of SPIE. 3431, 194–215, Airborne Reconnaissance XXII, SPIE.

Hecht, M.H., et al., 2008. Microscopy capabilities of the Microscopy, Electrochemistry, and Conductivity Analyzer. Journal of Geophysical Research 113, E00A22, http://dx.doi.org/10.1029/2008JE003077.

Heet, T.L., Arvidson, R.E., Cull, S.C., Mellon, M.T., Seelos, K.D., 2009. Geomorphic and geologic settings of the Phoenix lander mission landing site. Journal of Geophysical Research 114, E00E04, http://dx.doi.org/10.1029/2009JE003416.

Keller, H.U., Goetz, W., Hartwig, H., Hviid, S.F., Kramm, R., Markiewicz, W.J., Shinohara, C., Smith, P., Reynolds, R., Tanner, R., Woida, P., Woida, R., Bos, B.J., Lemmon, M.T., 2008. The Phoenix Robotic Arm Camera. J. Geophys. Res.-Planets 113, E00A17, http://dx.doi.org/10.1029/2007JE003044.

Leer, K., et al., 2008. Magnetic properties experiments and the Surface Stereo Imager calibration target onboard the Mars Phoenix 2007 Lander: design, calibration, and science goals. Journal of Geophysical Research 113, E00A16, http://dx.doi.org/10.1029/2007JE003014.

Milliken, R.E., Swayze, G.A., Arvidson, R.E., Bishop, J.L., Clark, R.N., Ehlmann, B.L., Green, R.O., Grotzinger, J.P., Morris, R.V., Murchie, S.L., Mustard, J.F., Weitz, C., 2008. Opaline silica in young deposits on Mars. Geology 36 (11), 847–850, http://dx.doi.org/10.1130/G24967A.1.

Milliken, R.E., Grotzinger, J.P., Thomson, B.J., 2010. Paleoclimate of Mars as captured by the stratigraphic record in Gale Crater. Geophysical Research Letters 37, L04201, http://dx.doi.org/10.1029/2009GL041870.

Morris, R.V., et al., 2006. Mössbauer mineralogy of rock, soil, and dust at Gusev crater, Mars: Spirit's journey through weakly altered olivine basalt on the plains and pervasively altered basalt in the Columbia Hills. Journal of Geophysical Research 111 E02S13 http://dx.doi.org/10.1029/2005JE002584.

Osborne, M.R., Crosby, N.T., 1987. Benzopyrenes. Cambridge Monographs on Cancer Research. University Press, Cambridge.

Pering, K.L., Ponnamperuma, C., 1971. Aromatic Hydrocarbons in the Murchison Meteorite. Science (New York, NY) 173, 237–239.

Robbins, M., 1994. Fluorescence. Gems and Minerals under Ultraviolet Light. Geoscience Press, Inc., Phoenix, Arizona.

Sidike, A., Wang, X.-M., Sawuti, A., Zhu, H.-J., Kusachi, I., Yamashita, N., 2006. Energy transfer among Pb, Ce and Mn in fluorescent calcite from Kuerle, Xinjiang, China. Physics and Chemistry of Minerals 33, 559–566, http://dx.doi.org/10.1007/s00269-006-0103-0.

Smith, H.D., Duncan, A.G., Neary, P.L., Lloyd, C.R., Anderson, A.J., Sims, R.C., McKay, C.P., 2012. In situ microbial detection in mojave desert soil using native fluorescence. Astrobiology 12 (3), 247–257, http://dx.doi.org/10.1089/ast.2010.0549.

Squyres, S.W., et al., 2008. Detection of silica-rich deposits on Mars. Science (New York, NY) 320, 1063–1067, http://dx.doi.org/10.1126/science.1155429.

Warren, T.S., Gleason, S., Bostwick, R.C., Verbeek, E.R., 1995. Ultraviolet Light and Fluorescent Minerals, Thomas S. Warren Publisher, Rio, West Virginia, ISBN: 0-9635098-0-2.

Yen, A.S., et al., 2005. An integrated view of the chemistry and mineralogy of martian soils. Nature 436, 49–54, http://dx.doi.org/10.1038/nature03637.

Zych, E., Goetz, W., Harrit, N., Spanggaard, H., 2004. Spectroscopic properties of sintered $BaMgAl_{10}O_{17}:Eu^{2+}$ (BAM) translucent pellets. Comparison to the commercial powder. Journal of Alloys and Compounds 380, 113–117.